# An internal electrode strategy for enhancing the stability and durability of triboelectric nanogenerator

Yibing Xie [a], Zihao Wang [b], Xiaoyue Ren [a], Maxwell Fordjour Antwi-Afari [c], Yameng Wang [a], Hao-Yang Mi [a] *, Bao Yang [b] *, Chuntai Liu [a]*, and Changyu Shen [a]

[a] *National Engineering Research Center for Advanced Polymer Processing Technology, Key Laboratory of Advanced Materials Processing and Mold of Ministry of Education, Zhengzhou University, Zhengzhou 450001, China*

[b] *School of Civil Engineering & Transportation, South China University of Technology, Guangzhou 510640, China*

[c] *Department of Civil Engineering, College of Engineering and Physical Sciences, Aston University, Birmingham, B4 7ET, UK*

---

\* Corresponding author.
\* Corresponding author.
\* Corresponding author.
*E-mail addresses:* mihaoyang@zzu.edu.cn (H.Y. Mi), byang20210415@scut.edu.cn (B. Yang), ctliu@zzu.edu.cn (C. Liu).

**ABSTRACT**

In this study, an internal electrode triboelectric nanogenerator (IE-TENG) design is proposed to enhance the stability, durability, and long-term performance of TENGs. By embedding a mesh-structured metal electrode in the friction layer, the IE-TENG becomes more flexible, lightweight, and robust than the traditional external electrode TENG (EE-TENG). When using copper mesh internal electrodes with higher grid density, the greater output can be achieved by comparing a series of polydimethylsiloxane(PDMS)-based IE-TENG. An equivalent output was obtained when using 60 copper mesh compared to EE-TENG, and the trend maintains for tribonegative low-density polyethylene (LDPE) and tribopositive polyamide (PA) polymers, which verifies the usability of the approach and the effective induction area of the internal electrode. The internal electrode design significantly enhanced the tolerance of the device to harsh environments and guaranteed excellent output stability. In addition, the IE-TENGs possess superior resistance to external interference and had about one time shorter saturation time for surface charges. As a demonstration, the IE-TENG can be used for collecting motion-sensing signals and detecting various sports activities. This study provides a novel strategy for the designing and customizing of highly integrated TENGs with enhanced durability for practical long-term applications.

*Keywords*: A: Flexible composites; A: Polymer-matrix composites (PMCs); B: Electrical properties

## 1. Introduction

As the world rapidly enters the new era of information technology, the demand for green and sustainable energy is growing. Triboelectric nanogenerators (TENGs) possess the merits of high electric-output performance, ease of fabrication, low cost, and high flexibility [1-7]. As a new type of wearable power source, it has made great progress in both academia and industry [8-13]. So far, various TENGs have been developed and demonstrated the ability to collect various energies, including wind [14-16], waves [17-19], human activities [1, 20-22], rain [23-25], and even weak vibration [26-28]. Furthermore, due to the portable size and flexibility of the TENGs, they can be used as self-powered sensors to detect various signals such as human-computer interaction [29-32], and tissue repair [33-35]. Typically, TENGs consist of multiple independent layers, including two triboelectric layers that generate opposite charges, and their corresponding electrodes can act as current collectors which are usually metal sheets [8-11, 17-21, 25-28, 36]. The complex structure and cumbersome assembly of TENGs make it challenging to achieve sustainable property and large-scale industrial production. Especially, the detachment of electrodes from the friction materials greatly hinders the practical application of TENGs in long-term or harsh environments, which is an urgent challenge for emerging wearable electronic devices.

To simplify the TENG structure, fabrication process, and improve device integration, several TENGs based on integrated conductive and polymer substrates without additional assembly processes have recently been developed [1, 37]. Due to their excellent mechanical properties and easy fusion with human skin, conductive hydrogels have become emerging materials for the preparation of wearable sensors and TENGs [38]. However, since its main component is water, which evaporates or freezes at sub-zero temperatures or dries at high temperatures over time, it causes conductive hydrogels to lose elasticity and conductivity, thus limiting its practical long-term application [39]. The introduction of organic solvents, such as glycerol into hydrogel networks, maybe a powerful strategy to address this challenge [40-45]. However, the

conductivity is reduced due to the reduction of water molecules [46]. To meet this challenge, encapsulation of conductive liquids [47, 48] or fiber networks [49] could be an alternative solution. However, there is a great risk of leakage due to the limitations of the packaging process. In addition, the use of hybrid and composite materials composed of inorganic conductive materials and organic elastic substrates is a feasible strategy. Conductive nanofillers, such as graphene [12, 50], carbon fiber [51], and carbon nanotubes [52, 53] have been embedded into the triboelectric elements through melt blending, solvent blending, and so on, to prepare conductive triboelectric materials. However, the cost of materials would be greatly enhanced, and the conductivity of the composites is usually low so that the current collectors are still used in many cases [46]. Moreover, the presence of conductive filler on the friction surface may unfavorably affect the triboelectric performance of the TENG.

In this study, we proposed a simple and effective method for the fabrication of highly compacted internal electrode TENG (IE-TENG). The metal mesh electrode embedded in the triboelectric element was used to prepare the metal-polymer composite. Compared with the traditional external electrode TENG (EE-TENG), it not only retains the high electrical conductivity of the metal but also greatly improves the flexibility. Moreover, it possesses excellent stability and durability which are more conducive to long-term applications. In addition, the electrodes in the IE-TENG have a better suppression effect with the friction layer for excessive deformation because of the greater contact area between the electrode and triboelectric material, which resulted in superior output consistency at different frequencies under the same load, especially for highly elastic materials like polydimethylsiloxane (PDMS). The influence of the internal electrode structure on the output performance and the underlying mechanisms were elucidated, whilst the internal electrode structure was optimized. The existence of the induced charge equivalence principle of IE-TENG was verified by different materials, e.g. low-density polyethylene (LDPE) and polyamide (PA). In addition, the IE-TENGs demonstrated better resistance to external interference and shorter surface charge

saturation time (up to one time) than traditional EE-TENGs. Moreover, the IE-TENG based on PA polymer was used as a self-powered sensor and exhibited reliable and stabilized motion-sensing signals. This study provides a new approach for the electrode design of highly stable and durable TENGs.

## 2. Experimental section

### 2.1. Materials

PDMS base elastomer (Sylgard 184A) and elastomer curing agent (Sylgard 184B) were purchased from Dow Corning (USA). TPU foam was obtained by the supercritical carbon dioxide foaming process provided by Shincell new material Co., Ltd (China). The copper mesh and the food-grade stainless steel meshes (SSM, Gb 304) with different mesh grids were purchased from Linqu Jielin environmental protection equipment Co., Ltd (China). The custom templates were purchased from Zhengzhou Craftsman Machinery Equipment Co., Ltd (China).

### 2.2. Experimental Setup for TENGs Performance Measurement

A field-emission scanning electron microscope (FE-SEM, Zeiss MERLIN Compact) was used to investigate the morphologies of the TPU foam. In addition, an electrometer (Keithley 6514) was used to measure the open-circuit voltages ($V_{oc}$), short-circuit current ($I_{sc}$), and short-circuit charge transfer ($Q_{sc}$) of IE-TENGs and EE-TENGs.

## 3. Results and discussion

To prepare the metal-polymer composites with an internal copper mesh, a mold composed of a square frame and two cover glasses was used as illustrated in Fig. 1a. PDMS precursor was poured into the frame with a copper mesh beneath it, followed by clamping using two cover glasses. The PDMS-copper mesh composite with a size of 5 cm × 5 cm and a thickness of 0.3 mm was obtained after curing at 100 ºC for 2 h (Fig. S1), and the precise control of the PDMS layer thickness was achieved by changing the thickness of the mold (Fig. S2). Fig. 1b shows

the cross-sectional diagram of the copper mesh embedded PDMS film (CEPF) in comparison with the copper sheet attached PDMS film (CAPF). It was found that the copper mesh was tightly bonded with the PDMS matrix for the CEPF, while a clear boundary (glue layer) was observed between the copper sheet and PDMS for CAPF. Due to the low surface energy and hydrophobicity of PDMS, the adhesion between PDMS and copper tape is low, which often resulted in the detachment of copper tape (Fig. S3). After about 15 repeated bending cycles, CEPF arose with no apparent surface damage as shown in Fig. 1c and Video 1. In contrast, significant creases caused by stress concentration appeared on the copper sheet of CAPF. In addition, CAPF can recover its original shape after the ultimate bending (bending angle 180º), indicating that the strategy of embedded electrode makes electrode and friction layer material perfectly compound and possess high flexibility (Video 2). When bending at the same angle (35º), the force required for 60-mesh CEPF (0.186 N) and 30-mesh CEPF (0.125N) is much less than that of CAPF (0.314 N) and 12-mesh CEPF (0.382 N) due to their thinner composing wires (Fig. S4). Thus, the IE-TENG could be easily bent showing good flexibility. To investigate the effect of the copper mesh on the output performance, different PDMS-copper mesh composites were prepared using copper meshes with 60, 30, and 12 meshes. A supercritical $CO_2$ foamed thermoplastic polyurethanes (TPU) sheet with a size of 3.5 cm × 3.5 cm and a thickness of 2 mm was used as the counterpart friction layer. The assembled TENG based on the metal-polymer composites with embedded metal mesh was named as internal electrode TENG (IE-TENG), while conventional TENG coated with conductive tape was named as external electrode TENG (EE-TENG). Fig. 1d shows the green fabrication process of porous TPU sheet preparation, in which a TPU film was placed in a high-pressure chamber followed by heating, $scCO_2$ saturation, rapid depressurization, and cooling. Fig. 1e presents the surface morphology of the TPU sheet, which possesses good flexibility and porous structure with an average pore size of ~112 μm (Tab. S1 and Fig. S5). Fig. 1f illustrates the cyclic compression curves of the foamed TPU sheet, which demonstrated small hysteresis loops in the

compression and releasing periods indicating excellent elasticity and resilience, which is favorable for providing high surface area and robust output performance.
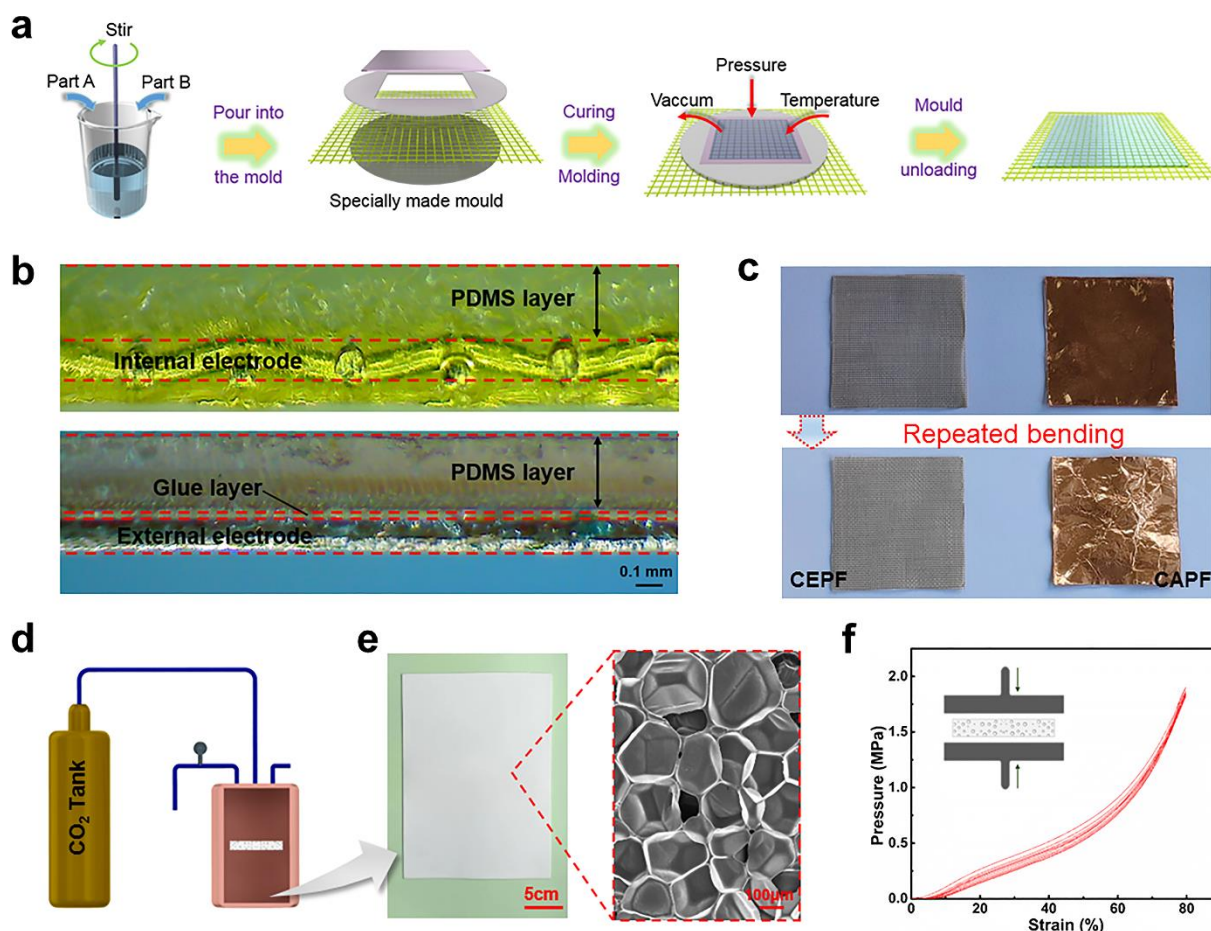


**Fig. 1.** a) Fabrication process of CEPF; b) Cross-sectional photographs of CEPF and CAPF; c) A comparison of the repeated bending between CEPF and CAPF; d) Illustration of the TPU foaming process; e) Photograph and SEM image of the TPU foam; f) Stress-strain curves in cyclic compression test of the TPU foam.

To explore the similarities and differences between the CEPF and CAPF, the TENGs were evaluated under different frequencies ranging from 1 to 3 Hz with a constant applied force of 15N. As shown in Fig. 2a, the Voc of EE-TENG and 60-mesh IE-TENG were similar at different frequencies. Both Voc can reach ~60 V under 1 Hz. It was found that the Voc decreases as the number of mesh decreases. The voltage of 12-mesh IE-TENG was ~30 V, which was only half of the output of the 60-mesh IE-TENG. Combined with the charge transfer

results (Fig. 2b), it was found that the trends of charge and voltage are consistent, which indicates that the total charge passing through the copper conductor decreases with the decrease of the number of mesh. In addition, four sets of Isc signals were enhanced about 2-3 times when the operation frequency was increased from 1 Hz to 3 Hz owing to the faster charge transfer rate at a higher frequency as shown in Fig. 2c [54-56]. Therefore, the current output rule of the IE-TENG conforms to Maxwell's displacement current theory [57]. The underlying influence mechanism of the internal mesh electrode structure on the output performance was elucidated. Fig. 2d illustrates the working principle of the IE-TENG, which is a typical single-electrode contact and separation working mode. When the TPU and CEPF are connected to each other, electrons are transferred from the TPU to the surface of the PDMS owing to their different electron-attracting abilities: (i) In the initial position, the CEPF is in full contact with the TPU, and the produced triboelectric charges with opposite polarities are balanced so that no electron flows in the external circuit; (ii) Once the TPU starts to separate from the CEPF, the negative charges on the surface of the PDMS induce positive charges on the internal electrode to reach an electrical equilibrium state. Thus, free electrons flow from the internal electrode to the ground, producing an output current signal; (iii) When the TPU continues to separate from the CEPF, the negative charges on the surface of the PDMS are fully screened from the induced positive charges on the internal electrode; and (iv) Once the TPU moves back to the CEPF, the induced positive charges on the internal electrode would decrease, which leads to the flow of free electrons from the ground to the internal electrode, thus a reverse output current signal could be observed. When the TPU comes in full contact with the CEPF again, the IE-TENG system returns to its initial state.

According to the actual size of the TENG, the corresponding simplified physical model is established (Tab. S2). The 3D morphology and the size labeling of the simplified model are created (Fig. S6 and Fig. S7). Then the triboelectric potential of the EE-TENG and IE-TENG with different CEPF mesh was simulated using ANSYS/Workbench software as shown in Fig.

2e. The simulation results indicated that the triboelectric potential of the PDMS and TPU did not vary significantly among four kinds of TENGs when the mesh number of CEPF was increased from 12 to 60, which implied the charge density generated on the friction layer surface was not affected by the configuration of the electrode and mesh number. Given that a decrease and increase in the triboelectric open voltage and charge transfer is directly related to the mesh number, it is inferred that the lack of an effective induction area of the internal copper mesh electrode may cause the reduction of induced charges on the electrode.
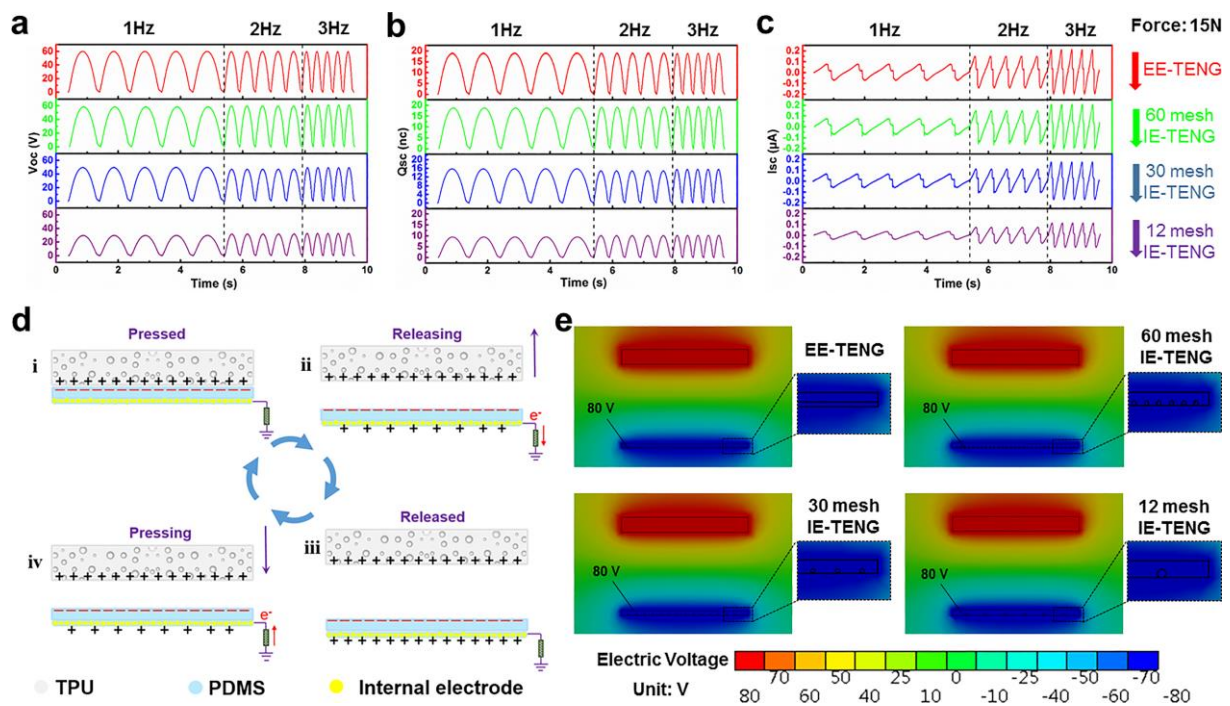


**Fig. 2.** a) $V_{oc}$, b) $Q_{sc}$, and c) $I_{sc}$ results of EE-TENG and IE-TENGs based on PDMS with different meshes at frequencies of 1, 2, and 3 Hz; d) Schematic illustration of the working mechanism of the PDMS-based IE-TENG; e) Simulation result of the static triboelectric potential distribution contrasted between EE-TENG and IE-TENGs based on PDMS with different meshes.

To further reveal the commonalities and differences between the four TENGs, we measured their output signals ($Q_{sc}$, $V_{oc}$, and $I_{sc}$), as the impact frequency varied from 1 to 3 Hz and

impact force from 5 to 65N (Fig. S8 – S11). It was surprisingly found that the output signal of EE-TENG and 60-mesh IE-TENG showed gradual differences with the increasing loading force. When the loading force reached 65 N, the charge transfer of both approaches to a stable value, and the voltage difference exceeds 5V. To observe the trend of each TENG more intuitively, the average Voc results of the four TENGs was counted with different applied force under a compression frequency of 1, 2, and 3 Hz, and the fitting curve is presented in Fig. 3a-c. When the same force was applied, the voltage output of the PDMS IE-TENG is basically consistent regardless of the frequency. Compared with the IE-TENG, the voltage output fluctuation of the EE-TENG increases with the increase of frequency, and the larger the loading force, the more obvious the phenomenon is. When the frequency was 1 Hz, the Voc of 60-mesh IE-TENG and EE-TENG began to differ at 35 N, but the mutation point changed to 25 N at 3Hz. Nevertheless, the Voc value was consistent before the mutation point under both frequencies. To further investigate the causes of this phenomenon, the simplified model was used for mechanical analysis. The cross-section of the strain cloud diagram shows that the internal electrode has a greater deformation limitation on PDMS film than the traditional externally attached electrode when 60 N external force was applied (Fig. 3d and Fig. S12). It was found that the strain change of CEPF was smaller than CAPF under the same boundary and load conditions, indicating that the internal copper mesh has a better deformation constraint on PDMS than the external copper tape. As an important factor affecting TENG output performance, the deformation ability of the friction material significantly affects the output performance and the reliability of the generated signal [58]. Under low frequency and small force, both CEPF and CAPF had negligible deformation in the PDMS layer. However, when the external force or frequency increases to a certain extent, the PDMS tends to deform due to its excellent elasticity. In the case of CAPF-based EE-TENG, a relatively large displacement will generate between PDMS and copper tape, while the internal electrode would constraint the elastic deformation of PDMS for the CEPF-

based IE-TENG, which results in less fluctuation in the output signal and more reliable performance.

Moreover, the trends of current and voltage signals are consistent for IE-TENG and EE-TENG at 3Hz (Fig. 3e). The $I_{sc}$ of 60-mesh IE-TENG showed a similar increasing trend when the applied pressure was increased from 4 to 36.7 kPa. While the improvement became insignificant when the applied pressure exceeded 36.7 kPa. Besides, the $I_{sc}$ of 60-mesh IE-TENG and EE-TENG began to differ at ~20.4 kPa. This may be because the internal electrode mode has better deformable binding to PDMS and can maintain better resilience and stability under high frequency and large external force. Conversely, the externally attached electrode has a poor deformation constraint on the PDMS at high frequencies and loads. In addition, the relevant radar map (Fig. 3f) made from the charge transfer data more clearly revealed the multiple relationships between the four TENGs. The total charge of 60-mesh IE-TENG is ~2.1 and ~1.3 times that of 12-mesh and 30-mesh IE-TENG, respectively. When the mesh number is small, the induced charge of the mesh electrode is in the undersaturation state concerning the total charge of the friction surface. When the mesh number reaches 60, the total induced charge output of PDMS-based IE-TENG and EE-TNEG can be regarded as an equivalent state, and IE-TENG possesses better output consistency and stability at different frequencies and high loads.
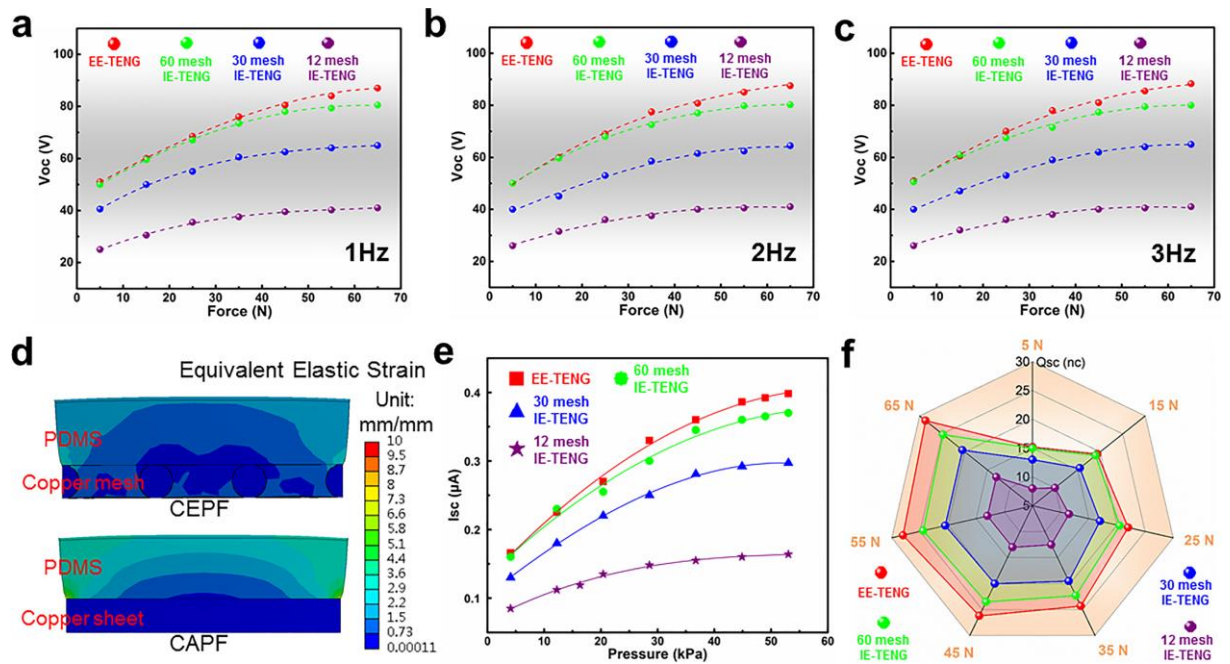
**Fig. 3.** Voc results of four TENGs been pressed using different compressive forces at a) 1Hz; b) 2Hz; c) 3Hz; d) Mechanical simulation model and results (cross-section view) of CEPF and CAPF; Fitting curves of the e) Isc results of four TENGs operated at different pressures; f) Qsc results of four TENGs operated at different forces.

To further verify the universal applicability of the internal electrode design of TENGs, two thermoplastic polymer materials with low elasticity (LDPE and PA), were selected to prepare copper mesh embedded LDPE film (CEPEF) and copper mesh embedded PA film (CEPAF). CEPF, CEPEF, and CEPAF were assembled with the same TPU foam as the counter friction layer to build contact-separation mode IE-TENGs. The charge transfer results recorded for different IE-TENGs were shown in Fig. 4a, depicting that the PDMS and LDPE tend to gain electrons to show negative charges, whereas PA is more tribopositive compared with TPU and showed positive charges. These results are coincident with the well-established tribo-series table [59]. The potential simulation results of LDPE EE-TENG, 60-mesh LDPE IE-TENG, PA EE-TENG, and 60-mesh PA IE-TENG are shown in Fig. 4b. It was found that the surface potential of the LDPE-based EE-TENG and IE-TENG are both ~ 29V, and it was ~ 7V for the

PA-based EE-TENG and IE-TENG, which means that the electrode structure was irrelevant to the surface charge generation property of the TENGs. Fig. 4c shows the Voc and Qsc statistical results of LDPE-based EE-TENG and IE-TENG at 3Hz. The Voc of LDPE-based EE-TENG and 60-mesh IE-TENG is highly consistent, indicating that the TENG of the two assembly modes has the same shape variable at high frequency and high force. Meanwhile, the charge induction of LDPE-based EE-TENG and 60-mesh IE-TENG are equivalent, and the Voc and Qsc decrease gradually with the decrease of the number of mesh. The Qsc of 60-mesh LDPE IE-TENG is 1.3 and 2.1 times that of 30-mesh and 12-mesh IE-TENG, respectively. These results and trends are consistent with the PDMS-based IE-TENG, which indicates that the charge induction is independent of the friction materials (Fig. S13). Moreover, the rule also applies to the output performance at 1Hz and 2Hz (Fig. S14). As shown in Fig. 4d and Tab. S3, when the pressure was increased from 4 to 36.7 kPa, the Isc of 60-mesh LDPE IE-TENG and LDPE EE-TENG had the same increasing trend and the slope of the fitting curve is basically the same. It proves that both have the same current output characteristics. In the case of PA-based EE-TENG and 60-mesh IE-TENG, the Voc, Isc, and Qsc were about the same under all applied forces (Fig. 4e and Fig. S15). In addition, the slopes of the current fitting curves are also quite close (Tab. S4), which means that the equivalent principle also applies to two positive friction materials. In addition, the results verified that different from elastic PDMS, the lateral displacement was unlikely to happen for plastic materials such as LDPE and PA.
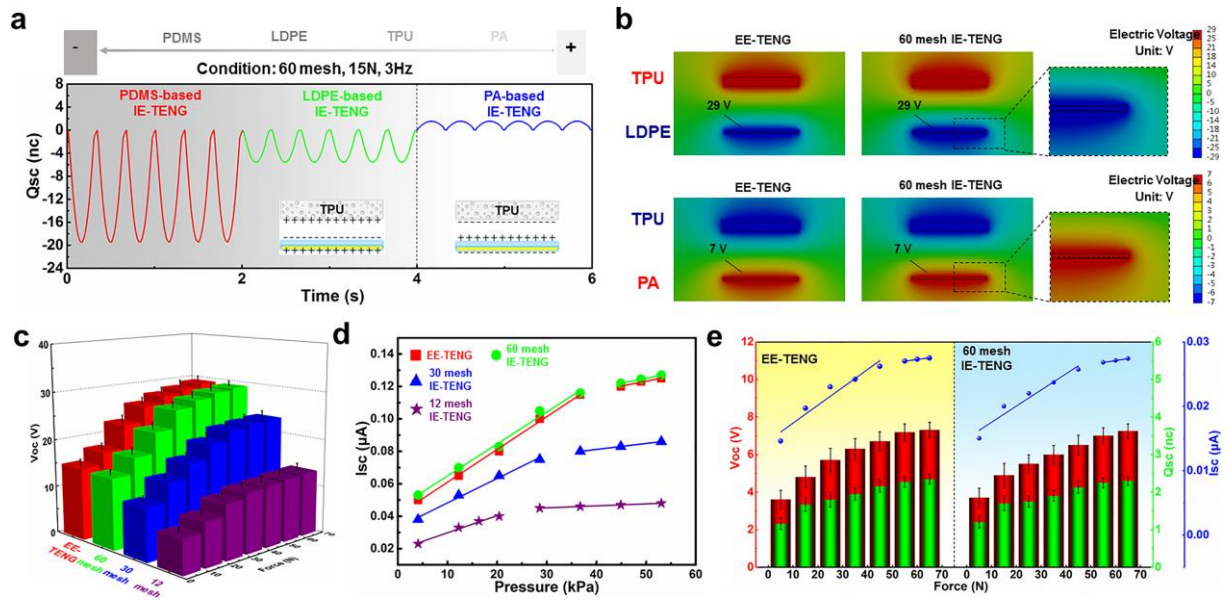
**Fig. 4.** a) Qsc vector signals of PDMS, LDPE, and PA-based IE-TENGs with 60-mesh internal electrode; b) The electric potential simulation results comparison of IE-TENGs based on LDPE and PA; c) Voc results of LDPE-based IE-TENGs; d) Isc results and fitting curves of different LDPE-based TENGs with different copper mesh; e) Voc, Qsc, and Isc statistical results and fitting curves of PA-based IE-TENG and EE-TENGs.

Next, we devote to elaborate on the underlying mechanism of the internal electrode structure on the output performance. In the case of EE-TENG, the charges generated on the copper sheets were induced by the electrostatic induction from the triboelectric materials as illustrated in Fig. 5a. According to the principle of charge induction, the surface-induced charges between two parallel plates of the same size are uniformly distributed [60]. Since the surface charge densities on the triboelectric surface were the same for both EE-TENG and IE-TENG, the number of induction charges generated on the copper mesh was the key to determine the output performance of IE-TENG. As shown in Fig. 5b and Fig. S16, the induction charges generated on the copper wires were affected by their dimension and their distance to the friction surface, as well as the inter-wire space. The induction effect on the back surface of the wire would be

weaker than the surface close to the friction surface [61, 62]. To sum up, for standard metal mesh, the larger the mesh number, the greater the effective induction area is, which could induced the more charges. When the mesh number exceeds 60, the induced charge on internal mesh electrode is equivalent to that can be induced on sheet electrode (Fig. S17). According to the results presented in Fig. 2, the induction charge on the CEPF was increased with the increase of the mesh grid of the copper mesh from 12 to 60 mesh, and the CEPF with 60 mesh demonstrated about the same output performance as the copper sheet, which means that the induced charges on the surface of copper mesh for IE-TENG were equivalent with the charges induced on the copper sheet for EE-TENG. In addition, it was found that the equivalent charge density achieved by the 60-mesh IE-TENG was ~1.3 times of the induced charge on the 30-mesh IE-TENG and ~2.1 times of the 12-mesh IE-TENG (Fig. 5b). These results and relationships should be valuable for explaining the influential factors for the IE-TENG and helpful for the design of IE-TENGs.

The basic FEM model of PDMS-based IE-TENG (dielectric-to-dielectric) is shown in Fig. 5c. According to Niu et al. [63], IE-TENG fundamentally can be equivalent to an electrostatic circuit system which consists of three capacitors, as shown in Fig. 5d. The output voltage under open-circuit condition (Voc) and the transferred charges under short-circuit condition (Qsc) have a relationship of Eq. (1):

$$Q_{sc} = V_{oc} C_0 \tag{1}$$

Where $C_0$ is the capacitance of the IE-TENG. When the moving TPU foam is in contact with PDMS film, Voc and Qsc are both 0. When the TPU foam is moving far away, Voc and Qsc can be derived as Eq. (2) (3):

$$V_{oc} = -\sigma A / 2C_0 \tag{2}$$

$$Q_{sc} = -\sigma A / 2 \tag{3}$$

Where σ is the density of electrostatic charges generated at the surface of the PDMS film and A is the effective contacting area between PDMS film and TPU foam. Furthermore, the copper mesh in the CEPF of IE-TENG was replaced with stainless steel mesh to study the influence of different internal electrode materials (Fig. S18). The resistance of the internal electrode was changed from 0.9 Ω to 1.9 Ω when the copper electrode is replaced with stainless steel electrode (Fig. S19). It was found that the Qsc, Voc, and Isc remained fairly consistent for both 60-mesh copper and stainless steel-based IE-TENG under different applied forces (Fig. S20). Thus, the metal type of the internal electrode embedded in the polymer matrix had a negligible effect on the output performance of IE-TENG. The principle of induced charge equivalence between mesh electrodes and plate electrodes applies to all kinds of metal electrodes. This conclusion is beneficial to extend the material selection of internal electrodes, which is conducive to guide the customization of IE-TENG according to different electrode requirements. In addition, the PDMS-based IE-TENG could charge a 0.1μF capacitor to 18 V, the LDPE-based IE-TENG could charge the capacitor to 10 V, and the PA-based IE-TENG could charge the capacitor to 3 V in 120 s through a bridge rectifier (Fig. S21). Moreover, they could easily light different numbers of LEDs (36 for PDMS-based IE-TENG, 13 for LDPE-based IE-TENG, and 4 for PA-based IE-TENG) by hand patting (Fig. S22). In addition, the weights of PDMS, LDPE, and PA-based IE-TENGs were measured in comparison with the corresponding EE-TENG. As shown in Fig. 5e, the IE-TENGs containing 60 mesh possess a relatively light overall weight than the corresponding EE-TENG for all three friction polymers. To investigate the durability of the IE-TENG, the IE-TENGs and EE-TENGs were soaked in salty water for 12 hours. Then, they were ultrasonic cleaned for 10 minutes and dried at 30 ºC to make sure no salt remains (Fig. S23). It was found that traditional external electrodes were mostly detached from the friction material due to the low adhesion of the glue layer (Tab. S5). In conclusion, all internal electrode friction layers maintained the same property suggesting that the internal electrode design has a good prevention effect on liquid erosion. The output

performance of PDMS-based EE-TENG and IE-TENG were measured before and after soaking. As shown in Fig. 5f, the Voc of IE-TENG was maintained the same before and after soaking, while the EE-TENG had a significant reduction in Voc. Therefore, the TENGs based on the internal electrode mode possess excellent tolerance to harsh environments and long-term stability, which leads to its greater advantages and prospects in practical applications compared with the TENG based on the external electrode.
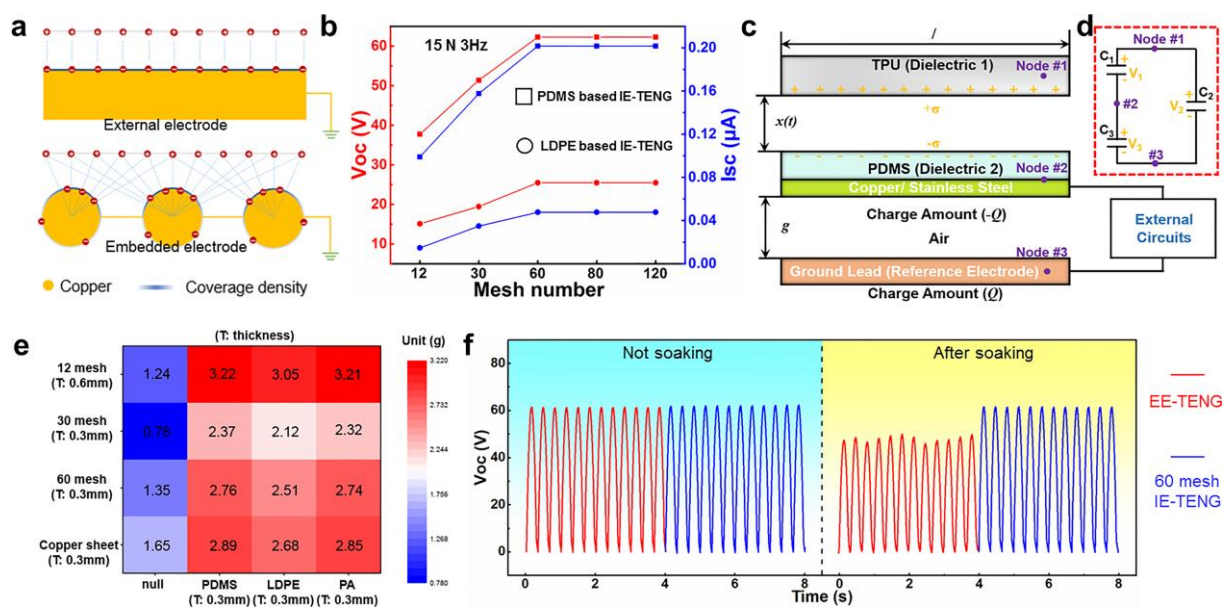


**Fig. 5.** The charge induction model proposed for a) EE-TENGs and IE-TENG; b) Voc and Isc change curve of IE-TENG with different mesh numbers of embedded mesh; c) Structure of the simplified model and d) equivalent circuit model containing three capacitances under open-circuit (OC) condition; e) The weight comparison of EE-TENG and IE-TENG; f) The Voc results of PDMS based IE-TENG and EE-TENG before and after soaking for 1 h.

Generally, surface charge saturation is a gradual process since the transfer of electrons between dissimilar materials usually does not occur instantly. The charges on the friction surface would gradually accumulate until saturating. The Voc signals of PDMS-based EE-TENG and IE-TENG were monitored from the first press cycle with a repetitive force of 25N

at 3Hz. As shown in Fig. 6a, it was found that it took a longer time for EE-TENG to reach a relatively stable signal than the other IE-TENGs, which means the internal electrodes TENG have a shorter surface charge saturation time than normally attached metal electrodes. Meanwhile, due to the high test accuracy of the electrometer (Keithley 6514), the baseline of Voc cycle signals is vulnerable to external interference [64]. After 5400 cycles of testing, the Voc baseline of IE-TENGs was more stable than that of EE-TENG, and the saturation time for IE-TENGs made of CPEF with different mesh was about the same. Moreover, a similar trend was observed in the case of LDPE and PA-based IE-TENG and EE-TENG (Fig. 6b and c). Hence, the internal electrode design could not only reach the stable voltage peak faster, but also has better stability than the traditional external electrode design (Fig. S24). Therefore, this study speculates that it possesses a unique protection mechanism in IE-TENGs to effectively resist external signal interference, which is due to the highly integrated electrode and triboelectric material.

With these favorable attributes, this study sets a specific scene to demonstrate the performance of the IE-TENG as a self-powered sensor. Since PA has excellent wear resistance, the IE-TENG based on PA was used as a self-powered sensor to monitor the behavior during skateboarding and snowboarding. Fig. S25 shows the design concept diagram, the highly integrated CEPAF composite (positive friction layer) and shock-absorbing TPU foam sole (negative friction layer) form a wearable device for real-time monitoring. The results are displayed in Fig. 6d-f and movie 3, different signal patterns were obtained when the tester simulated different actions according to the characteristics of different projects. Skateboarding can be regarded as a process of repeated contact and separation between the sole and the skateboard. When we test the skateboard model, we can detect a stable voltage signal, whose value is ~7 V, which is highly consistent with the previous simulation and test results. In skiing, shoes and skis are fixed together, the main monitored behavior is the extrusion of the skiing surface in the process of walking and the vibration generated in the process of jumping. Through

the simulation test, the peaks and lines shape of the two voltage signals have high identification. In addition, the PA-based IE-TENGs could maintain about the same Voc signal when running at -20 ºC as the room temperature, which proves that the IE-TENGs possess good sensing performance at low temperature (Fig. S26). In summary, even though the electrical properties of PA and TPU are similar, Voc signals corresponding to different action types can be easily obtained and distinguished. Moreover, the detected signals show high stability.
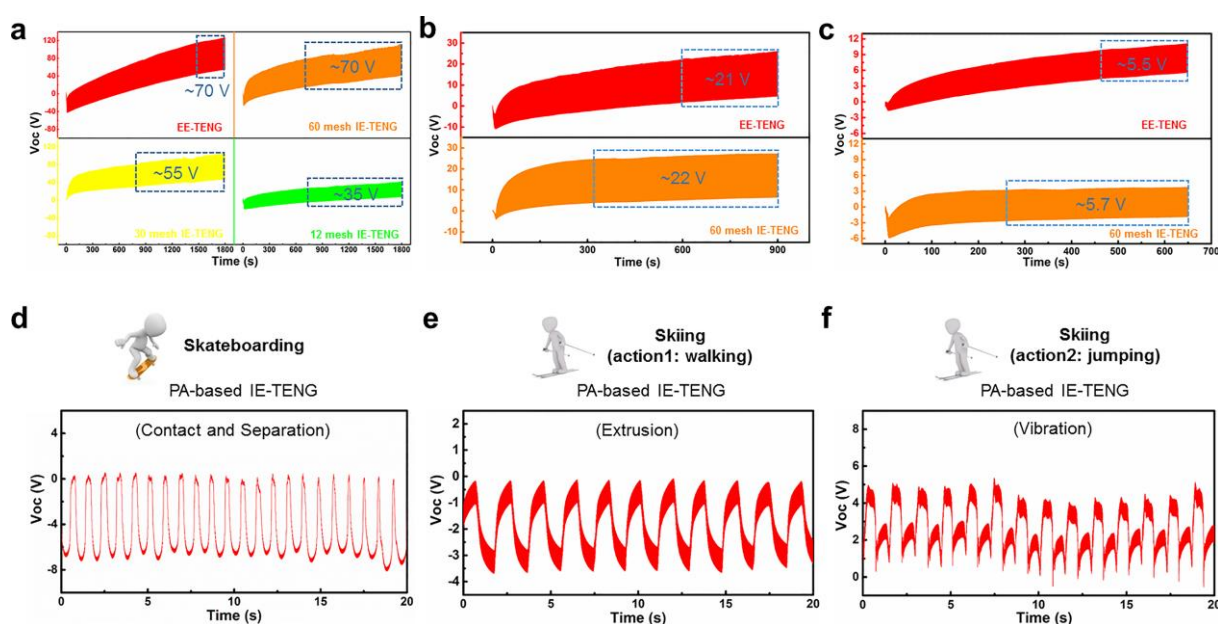


**Fig. 6.** a) The contrast of open voltage for PDMS-based EE-TENG and IE-TENGs with various electrode configurations; b) The contrast of open voltage for LDPE-based EE-TENG and 60-mesh IE-TENG; c) The contrast of open voltage for PA-based EE-TENG and 60 mesh IE-TENG; d-f) Detecting different behavior of human using a 60-mesh IE-TENG based on PA placed on the skateboards and skis (The other friction layer is TPU foam sole).

## 4. Conclusions

A simple environmentally friendly approach was proposed to fabricate IE-TENGs with mesh-structured electrodes embedded in the friction material. This design not only solves the low adhesion of the commercial metallic tape to the friction layer, but also avoids the erosion

of traditional external electrodes. The output performance of IE-TENGs based on PDMS showed an increasing trend with the increase of mesh grid and the 60-mesh copper electrode achieved equivalent output with traditional EE-TENG. It was found that the electrostatic charges induced on the metal mesh were the main factor influencing the output performance, and the output could be enhanced by enlarging the effect charge induction area of the internal electrode. Due to the enclosed design of the IE-TENG, it demonstrated flexibility, lightweight characteristic, more stable long-term signals, and high tolerance to the harsh environment. Besides PDMS, the trends found are widely applicable to various polymers as verified by tribonegative LDPE and tribopositive PA. In addition, IE-TENG has about one time faster surface charge saturation rate than traditional EE-TENG, which contributed to its superior stability and faster response. As a demonstration, the IE-TENG was used as a self-powered sensor to detect the posture and sense different movements in various sports. This work provides a new IE-TENG design and its fundamental properties, which are expected to be useful for the development of highly stable and durable TENG for practical applications.

## Declaration of Competing Interest

The authors declare that they have no known competing financial interests or personal relationships that could have appeared to influence the work reported in this paper.

## Acknowledgments

# References

[1] J. Luo, W. Gao, Z.L. Wang, The Triboelectric Nanogenerator as an Innovative Technology toward Intelligent Sports, Adv Mater 33(17) (2021) e2004178.

[2] B. Chen, Z.L. Wang, Toward a New Era of Sustainable Energy: Advanced Triboelectric Nanogenerator for Harvesting High Entropy Energy, Small (2022) e2107034.

[3] L. Lu, C. Jiang, G. Hu, J. Liu, B. Yang, Flexible Noncontact Sensing for Human-Machine Interaction, Adv Mater 33(16) (2021) e2100218.

[4] N. Wang, W. Zhang, Z. Li, S. Wang, A. Suwardi, E. Ye, B. Li, Y. Liu, Z. Wu, Y. Dong, X. J. Loh, D. Wang, Dual-electric-polarity augmented cyanoethyl cellulose-based triboelectric nanogenerator with ultra-high triboelectric charge density and enhanced electrical output property at high humidity, Nano Energy 103 (2022) 107748.

[5] J. H. Choi, Y. Ra, S. Cho, M. La, S. J. Park, D. Choi, Electrical charge storage effect in carbon based polymer composite for long-term performance enhancement of the triboelectric nanogenerator, Composites Science and Technology 207 (2021) 108680.

[6] N. Wang, Y. Liu, E. Ye, Z. Li, D. Wang, Control methods and applications of interface contact electrification of triboelectric nanogenerators: a review, Materials Research Letters, 10(3) (2022) 97-123.

[7] N. Wang, Y. Liu, Y. Wu, Z. Li, D. Wang, A β-cyclodextrin enhanced polyethylene terephthalate film with improved contact charging ability in a high humidity environment, Nanoscale Advances 3(21) (2021) 6063-6073.

[8] F. Peng, D. Liu, W. Zhao, G. Zheng, Y. Ji, K. Dai, L. Mi, D. Zhang, C. Liu, C. Shen, Facile fabrication of triboelectric nanogenerator based on low-cost thermoplastic polymeric fabrics for large-area energy harvesting and self-powered sensing, Nano Energy 65 (2019).

[9] Y. Hao, J. Wen, X. Gao, D. Nan, J. Pan, Y. Yang, B. Chen, Z.L. Wang, Self-Rebound Cambered Triboelectric Nanogenerator Array for Self-Powered Sensing in Kinematic Analytics, ACS Nano (2022).

[10] P. Manchi, S. A. Graham, B. Dudem, H. Patnam, J. S. Yu, Improved performance of nanogenerator via synergetic piezo/triboelectric effects of lithium niobate microparticles embedded composite films, Composites Science and Technology 201 (2021) 108540.

[11] Q. Zhang, T. Jin, J. Cai, L. Xu, T. He, T. Wang, Y. Tian, L. Li, Y. Peng, C. Lee, Wearable Triboelectric Sensors Enabled Gait Analysis and Waist Motion Capture for IoT-Based Smart Healthcare Applications, Adv Sci (Weinh) 9(4) (2022) e2103694.

[12] K. Zhou, Y. Zhao, X. Sun, Z. Yuan, G. Zheng, K. Dai, L. Mi, C. Pan, C. Liu, C. Shen, Ultra-stretchable triboelectric nanogenerator as high-sensitive and self-powered electronic skins for energy harvesting and tactile sensing, Nano Energy 70 (2020).

[13] P. Hu, L.Yan, C. Zhao, Y. Zhang, J. Niu, Double-layer structured PVDF nanocomposite film designed for flexible nanogenerator exhibiting enhanced piezoelectric output and mechanical property, Composites Science and Technology 168 (2018) 327-335.

[14] Z. Zhao, X. Pu, C. Du, L. Li, C. Jiang, W. Hu, Z.L. Wang, Freestanding Flag-Type Triboelectric Nanogenerator for Harvesting High-Altitude Wind Energy from Arbitrary Directions, ACS Nano 10(2) (2016) 1780-7.

[15] L. Zhang, B. Zhang, J. Chen, L. Jin, W. Deng, J. Tang, H. Zhang, H. Pan, M. Zhu, W. Yang, Z.L. Wang, Lawn Structured Triboelectric Nanogenerators for Scavenging Sweeping Wind Energy on Rooftops, Adv Mater 28(8) (2016) 1650-6.

[16] B. Chen, Y. Yang, Z.L. Wang, Scavenging Wind Energy by Triboelectric Nanogenerators, Advanced Energy Materials 8(10) (2018).

[17] X. Wang, S. Niu, Y. Yin, F. Yi, Z. You, Z.L. Wang, Triboelectric Nanogenerator Based on Fully Enclosed Rolling Spherical Structure for Harvesting Low-Frequency Water Wave Energy, Advanced Energy Materials 5(24) (2015).

[18] Y. Su, X. Wen, G. Zhu, J. Yang, J. Chen, P. Bai, Z. Wu, Y. Jiang, Z. Lin Wang, Hybrid triboelectric nanogenerator for harvesting water wave energy and as a self-powered distress signal emitter, Nano Energy 9 (2014) 186-195.

[19] F. Shen, Z. Li, H. Guo, Z. Yang, H. Wu, M. Wang, J. Luo, S. Xie, Y. Peng, H. Pu, Recent Advances towards Ocean Energy Harvesting and Self-Powered Applications Based on Triboelectric Nanogenerators, Advanced Electronic Materials 7(9) (2021).

[20] J. Zhu, Y. Zhang, G. Zheng, Y. Ji, K. Dai, L. Mi, D. Zhang, C. Liu, C. Shen, Microribbon Structured Polyvinylidene Fluoride with High-Performance Piezoelectricity for Sensing Application, ACS Applied Polymer Materials 3(5) (2021) 2411-2419.

[21] N. Wang, D. Yang, W. Zhang, M. Feng, Z. Li, E. Ye, X. J. Loh, D. Wang, Deep trap boosted ultrahigh triboelectric charge density in nanofibrous cellulose-based triboelectric nanogenerators, ACS Appl Mater Interfaces 15 (2023) 997-1009.

[22] Y. Xie, J. Hu, H. Li, H.-Y. Mi, G. Ni, X. Zhu, X. Jing, Y. Wang, G. Zheng, C. Liu, C. Shen, Green fabrication of double-sided self-supporting triboelectric nanogenerator with high durability for energy harvesting and self-powered sensing, Nano Energy 93 (2022).

[23] H.R. Zhu, W. Tang, C.Z. Gao, Y. Han, T. Li, X. Cao, Z.L. Wang, Self-powered metal surface anti-corrosion protection using energy harvested from rain drops and wind, Nano Energy 14 (2015) 193-200.

[24] X. Liu, P. Cui, J. Wang, W. Shang, S. Zhang, J. Guo, G. Gu, B. Zhang, G. Cheng, Z. Du, A robust all-inorganic hybrid energy harvester for synergistic energy collection from sunlight and raindrops, Nanotechnology 32(7) (2021) 075401.

[25] F. Peng, M. Gao, Z. Han, D. Liu, K. Dai, L. Mi, D. Zhang, G. Zheng, C. Liu, C. Shen, One-step fabrication of sandwiched film based triboelectric nanogenerator for large-area energy harvester and precise self-powered sensor, Nano Energy 103 (2022).

[26] H.-Y. Mi, X. Jing, Q. Zheng, L. Fang, H.-X. Huang, L.-S. Turng, S. Gong, High-performance flexible triboelectric nanogenerator based on porous aerogels and electrospun nanofibers for energy harvesting and sensitive self-powered sensing, Nano Energy 48 (2018) 327-336.

[27] Z. Wang, Y. Wu, W. Jiang, Q. Liu, X. Wang, J. Zhang, Z. Zhou, H. Zheng, Z. Wang, Z.L.

Wang, A Universal Power Management Strategy Based on Novel Sound‑Driven Triboelectric Nanogenerator and Its Fully Self‑Powered Wireless System Applications, Advanced Functional Materials 31(34) (2021).

[28] X. Huang, J. Li, Y. Liu, T. Wong, J. Su, K. Yao, J. Zhou, Y. Huang, H. Li, D. Li, M. Wu, E. Song, S. Han, X. Yu, Epidermal self-powered sweat sensors for glucose and lactate monitoring, Bio-Design and Manufacturing (2022) 1-9.

[29] M. Li, Y. Zhang, L. Lian, K. Liu, M. Lu, Y. Chen, L. Zhang, X. Zhang, P. Wan, Flexible Accelerated‑Wound‑Healing Antibacterial MXene‑Based Epidermic Sensor for Intelligent Wearable Human‑Machine Interaction, Advanced Functional Materials (2022).

[30] S. Parandeh, N. Etemadi, M. Kharaziha, G. Chen, A. Nashalian, X. Xiao, J. Chen, Advances in Triboelectric Nanogenerators for Self‑Powered Regenerative Medicine, Advanced Functional Materials 31(47) (2021).

[31] B. Lan, F. Wu, Y. Cheng, Y. Zhou, G. Hossain, G. Grabher, L. Shi, R. Wang, J. Sun, Scalable, stretchable and washable triboelectric fibers for self-powering human-machine interaction and cardiopulmonary resuscitation training, Nano Energy 102 (2022).

[32] G. Conta, A. Libanori, T. Tat, G. Chen, J. Chen, Triboelectric Nanogenerators for Therapeutic Electrical Stimulation, Advanced Materials 33(26) (2021).

[33] S. Yao, M. Zheng, Z. Wang, Y. Zhao, S. Wang, Z. Liu, Z. Li, Y. Guan, Z.L. Wang, L. Li, Self-powered, Implantable, and Wirelessly-Controlled NO Generation System for Intracranial Neuroglioma Therapy, Adv Mater (2022) 2205881.

[34] P. Chen, C. Xu, P. Wu, K. Liu, F. Chen, Y. Chen, H. Dai, Z. Luo, Wirelessly Powered Electrical-Stimulation Based on Biodegradable 3D Piezoelectric Scaffolds Promotes the Spinal Cord Injury Repair, ACS Nano (2022).

[35] F. Yi, Z. Zhang, Z. Kang, Q. Liao, Y. Zhang, Recent Advances in Triboelectric Nanogenerator‑Based Health Monitoring, Advanced Functional Materials 29(41) (2019).

[36] C. Sukumaran, V. Vivekananthan, V. Mohan, Z.C. Alex, A. Chandrasekhar, S.-J. Kim, Triboelectric nanogenerators from reused plastic: An approach for vehicle security alarming and tire motion monitoring in rover, Applied Materials Today 19 (2020).

[37] Q. Zhang, C. Xin, F. Shen, Y. Gong, Y. Zi, H. Guo, Z. Li, Y. Peng, Q. Zhang, Z.L. Wang, Human body IoT systems based on the triboelectrification effect: energy harvesting, sensing, interfacing and communication, Energy & Environmental Science 15(9) (2022) 3688-3721.

[38] L. Sun, S. Chen, Y. Guo, J. Song, L. Zhang, L. Xiao, Q. Guan, Z. You, Ionogel-based, highly stretchable, transparent, durable triboelectric nanogenerators for energy harvesting and motion sensing over a wide temperature range, Nano Energy 63 (2019).

[39] L.-B. Huang, X. Dai, Z. Sun, M.-C. Wong, S.-Y. Pang, J. Han, Q. Zheng, C.-H. Zhao, J. Kong, J. Hao, Environment-resisted flexible high performance triboelectric nanogenerators based on ultrafast self-healing non-drying conductive organohydrogel, Nano Energy 82 (2021).

[40] Y. Hong, Z. Lin, Z. Luo, T. Jiang, J. Shang, Y. Yang, Development of conductive hydrogels: from design mechanisms to frontier applications, Bio-Design and Manufacturing 5(4) (2022) 729-756.

[41] Y. Wei, L. Xiang, H. Ou, F. Li, Y. Zhang, Y. Qian, L. Hao, J. Diao, M. Zhang, P. Zhu, Y. Liu, Y. Kuang, G. Chen, MXene-Based Conductive Organohydrogels with Long-Term Environmental Stability and Multifunctionality, Advanced Functional Materials 30(48) (2020).

[42] X. Liu, Z. Wu, D. Jiang, N. Guo, Y. Wang, T. Ding, L. Weng, A highly stretchable, sensing durability, transparent, and environmentally stable ion conducting hydrogel strain sensor built by interpenetrating Ca2+-SA and glycerol-PVA double physically cross-linked networks, Adv Compos Hybrid Mater 5 (2022) 1712-1729.

[43] H. Chen, X. Ren, G. Gao, Skin-Inspired Gels with Toughness, Antifreezing, Conductivity, and Remoldability, ACS Appl Mater Interfaces 11(31) (2019) 28336-28344.

[44] L. Han, K. Liu, M. Wang, K. Wang, L. Fang, H. Chen, J. Zhou, X. Lu, Mussel-Inspired Adhesive and Conductive Hydrogel with Long-Lasting Moisture and Extreme Temperature

Tolerance, Advanced Functional Materials 28(3) (2018).

[45] H. Liao, X. Guo, P. Wan, G. Yu, Conductive MXene Nanocomposite Organohydrogel for Flexible, Healable, Low‑Temperature Tolerant Strain Sensors, Advanced Functional Materials 29 (39) (2019) 1904507.

[46] H. Sun, Y. Zhao, S. Jiao, C. Wang, Y. Jia, K. Dai, G. Zheng, C. Liu, P. Wan, C. Shen, Environment Tolerant Conductive Nanocomposite Organohydrogels as Flexible Strain Sensors and Power Sources for Sustainable Electronics, Advanced Functional Materials 31(24) (2021).

[47] L. Wang, W. Liu, Z. Yan, F. Wang, X. Wang, Stretchable and Shape‑Adaptable Triboelectric Nanogenerator Based on Biocompatible Liquid Electrolyte for Biomechanical Energy Harvesting and Wearable Human–Machine Interaction, Advanced Functional Materials 31(7) (2020).

[48] R. Liu, X. Kuang, J. Deng, Y.-C. Wang, A.C. Wang, W. Ding, Y.-C. Lai, J. Chen, P. Wang, Z. Lin, H.J. Qi, B. Sun, Z.L. Wang, Shape Memory Polymers for Body Motion Energy Harvesting and Self-Powered Mechanosensing, Advanced Materials 30(8) (2018).

[49] Y.C. Lai, J. Deng, S. Niu, W. Peng, C. Wu, R. Liu, Z. Wen, Z.L. Wang, Electric Eel-Skin-Inspired Mechanically Durable and Super-Stretchable Nanogenerator for Deformable Power Source and Fully Autonomous Conformable Electronic-Skin Applications, Adv Mater 28(45) (2016) 10024-10032.

[50] Y. Wang, H. Wu, L. Xu, H. Zhang, Y. Yang, Z.L. Wang, Hierarchically patterned self-powered sensors for multifunctional tactile sensing, Science Advances 6(34) (2020) eabb9083.

[51] Y. Shao, C. Luo, B.-w. Deng, B. Yin, M.-b. Yang, Flexible porous silicone rubber-nanofiber nanocomposites generated by supercritical carbon dioxide foaming for harvesting mechanical energy, Nano Energy 67 (2020).

[52] Y.J. Fan, X.S. Meng, H.Y. Li, S.Y. Kuang, L. Zhang, Y. Wu, Z.L. Wang, G. Zhu, Stretchable Porous Carbon Nanotube-Elastomer Hybrid Nanocomposite for Harvesting Mechanical Energy,

Adv Mater 29(2) (2017).

[53] S. Chen, T. Huang, H. Zuo, S. Qian, Y. Guo, L. Sun, D. Lei, Q. Wu, B. Zhu, C. He, X. Mo, E. Jeffries, H. Yu, Z. You, A Single Integrated 3D-Printing Process Customizes Elastic and Sustainable Triboelectric Nanogenerators for Wearable Electronics, Advanced Functional Materials 28(46) (2018).

[54] Y. Shao, C.-p. Feng, B.-w. Deng, B. Yin, M.-b. Yang, Facile method to enhance output performance of bacterial cellulose nanofiber based triboelectric nanogenerator by controlling micro-nano structure and dielectric constant, Nano Energy 62 (2019) 620-627.

[55] J. Qian, J. He, S. Qian, J. Zhang, X. Niu, X. Fan, C. Wang, X. Hou, J. Mu, W. Geng, X. Chou, A Nonmetallic Stretchable Nylon‑Modified High Performance Triboelectric Nanogenerator for Energy Harvesting, Advanced Functional Materials 30(4) (2019).

[56] C. Ning, K. Dong, R. Cheng, J. Yi, C. Ye, X. Peng, F. Sheng, Y. Jiang, Z.L. Wang, Flexible and Stretchable Fiber‑Shaped Triboelectric Nanogenerators for Biomechanical Monitoring and Human‑Interactive Sensing, Advanced Functional Materials 31(4) (2020).

[57] Z.L. Wang, On Maxwell's displacement current for energy and sensors: the origin of nanogenerators, Materials Today 20(2) (2017) 74-82.

[58] S. Wang, L. Lin, Z.L. Wang, Nanoscale triboelectric-effect-enabled energy conversion for sustainably powering portable electronics, Nano Lett 12(12) (2012) 6339-46.

[59] Z.L. Wang, A.C. Wang, On the origin of contact-electrification, Materials Today 30 (2019) 34-51.

[60] Q. Wang, M. Chen, W. Li, Z. Li, Y. Chen, Y. Zhai, Size effect on the output of a miniaturized triboelectric nanogenerator based on superimposed electrode layers, Nano Energy 41 (2017) 128-138.

[61] W. Lin, The electrostatic images of a dielectric sphere. Journal of Electrostatic 36 (1995) 129-137.

[62] W.T. Norris, Charge images in a dielectric sphere. IEE Proceedings-Science, Measurement and Technology 142(2) (1995): 142-150.

[63] S. Niu, Z.L. Wang, Theoretical systems of triboelectric nanogenerators, Nano Energy 14 (2015) 161-192.

[64] J. An, P. Chen, C. Li, F. Li, T. Jiang, Z.L. Wang, Methods for correctly characterizing the output performance of nanogenerators, Nano Energy 93 (2022).